ACS OMEGA

http://pubs.acs.org/journal/acsodf

Article

Synthesis and Electrochemical Performance of KVO/GO Composites as Anodes for Aqueous Rechargeable Lithium-Ion Batteries

Wenyuan Duan, Yanlin Li,* Youyang Zhao, Huimin Zhang, Jiao Liu, Yuzhen Zhao,* and Zongcheng Miao*

Cite This: *ACS Omega* 2022, 7, 35552−35561

Read Online

ACCESS | Metrics & More | Article Recommendations | Supporting Information

ABSTRACT: $K_{0.25}V_2O_5$ (KVO) and $K_{0.25}V_2O_5$/graphene oxide (KVO/GO) have been successfully synthesized by a chemical coprecipitation method and a subsequent calcination process. The structure and morphology of KVO and KVO/GO were characterized by X-ray diffraction, scanning electron microscopy, transmission electron microscopy, and X-ray photoelectron spectroscopy. The as-obtained vanadate and vanadate modified by GO materials were used as anodes with $LiMn_2O_4$ as a cathode and saturated $LiNO_3$ as an electrolyte to assemble an aqueous rechargeable lithium-ion battery (ARLB). The cyclic voltammogram curves of both KVO and KVO/GO electrodes exhibited three pairs of redox peaks corresponding to charge/discharge platforms. We found that a small amount of graphene oxide added improved the electrochemical performance more significantly than excess graphene oxide. The as-prepared KVO/GO//$LiMn_2O_4$ could not only improve the initial discharge capacity but could also reduce the attenuation at a high current density. Furthermore, the ARLB with a KVO/GO anode exhibited an excellent rate performance and super long cycle life. These good electrochemical properties of this new ARLB system actually provided feasibility for application in large-scale power sources and energy storage devices.

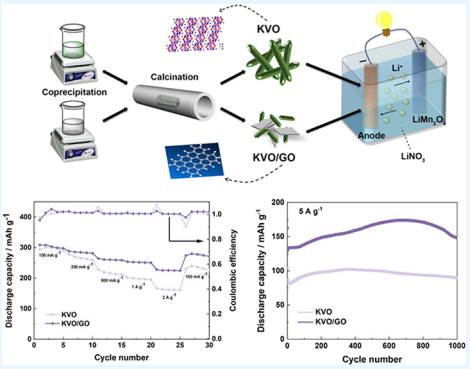

1. INTRODUCTION

Nowadays, traditional lithium-ion batteries (LIBs) with organic electrolytes are widely used in portable equipment, electronic products, and power storage owing to their high energy capacity, long cycle life, and good temperature resistance. However, problems have been exposed frequently in terms of LIB incidents in recent years because of flammable organic electrolytes, such as the explosion of Samsung Galaxy Note 7, fire of Tesla Model S, and spontaneous combustion at a lithium-ion battery storage plant in Beijing, which sounds an alarm for safety of traditional LIBs. Moreover, organic electrolytes are expensive and toxic, which greatly limits the development of LIBs.[1−3]

Fortunately, aqueous rechargeable lithium-ion batteries (ARLBs) have been proven to be safe, low-cost, and environmentally friendly alternatives that can provide a high efficiency and long life for power applications.[4,5] Some cheap and nontoxic inorganic electrolytes such as $LiNO_3$, LiCl, and Li_2SO_4 solutions[6−11] have been commonly used in ARLBs because they exhibit significant advantages in having a large dielectric constant, low viscosity, high dissociating function, and small migration resistance, leading to a higher ionic conductivity than that of LIBs. It is of importance that ARLBs could provide a fast charge/discharge process at a large current density, which probably makes it the next generation of power sources and energy devices.

In the system of ARLBs, $LiFePO_4$, Li_2MnO_3, $LiMn_2O_4$, and $LiCoO_2$[3,12−17] as the cathode materials have been widely investigated due to their high discharge capacity, good rate capability, and cycle performance. However, the choice of anode materials remained a challenge because traditional carbon materials as anodes exhibited poor cycle life and low capacity due to dramatic volume and structure changes. A new study showed that vanadate has a large theoretical capacity, long cycle stability, excellent kinetics, and low cost,[18] which is a promising kind of anode material to be applied in ARLBs. He et al. introduced the structure, operation mechanism, and synthesis of LiV_3O_8 anodes and then studied the modification methods to improve their performance by coating modification, introducing a conductive agent, ion doping, and nanocrystallization.[19] Zhao et al. formed $Na_{0.8}K_{0.2}V_6O_{15}$ crystals as ARLB anodes that exhibited an efficient discharge capacity retaining 61% over 50 cycles[20] and further studied $Na_{0.8}K_{0.2}V_6O_{15}$@V_2O_5 to obtain a 54.1% capacity retained over 60 cycles.[21] Xie et al. reported the synthesis of CuV_2O_5

Received: May 7, 2022
Accepted: September 2, 2022
Published: September 26, 2022

https://doi.org/10.1021/acsomega.2c02833
ACS Omega 2022, 7, 35552−35561

Table 1. Characteristics and Electrochemical Performance of Various Vanadate Anode Materials in Different Works

materials	characteristic morphology	counter electrode	electrolyte	1st discharge capacity (mAh g^{-1})	cycling discharge capacity (n^{th}) (mAh g^{-1})
$Na_{0.8}K_{0.2}V_6O_{15}$[20]	nanorods	nickel mesh	saturated $LiNO_3$ solution	218	133 (50th) at 100 mA g^{-1}
$Na_{0.8}K_{0.2}V_6O_{15}$@ V_2O_5[21]	nanorods	nickel mesh	saturated $LiNO_3$ solution	151.1	113.0 (60th) at 3 A g^{-1}
CuV_2O_5[22]	nanobelts	$LiMn_2O_4$	5 M $LiNO_3$ + 0.001 M LiOH	130.6	68.6 (50th) at 60 mA g^{-1}
NaV_6O_{15}[23]	nanoflakes	$LiMn_2O_4$	2 mol/L Li_2SO_4	110.7	90% (100th) at 300 mA g^{-1}
LiV_3O_8[24]	layer structure	$LiMn_2O_4$	2 mol/L Li_2SO_4	59	29.5 (100th) at 0.2C
V_2O_5/PPy[25]	nanowires/CNT	$LiMn_2O_4$	0.5 mol/L $LiSO_4$	118	112 (500th) at 200 mA g^{-1}
$(NH_4)_2V_7O_{16}$[26]	microbricks	platinum sheet	2 mol/L Li_2SO_4 + 1 mol/L Na_2SO_4	43.92	37.71 (500th) at 100 mA g^{-1}
$NH_4V_4O_{10}$[27]	layered frame	nickel mesh	saturated $LiNO_3$ solution	187.66	60.7 (200th) at 2 A g^{-1}
LiV_3O_8[28]	nanowires	$LiMn_2O_4$	saturated $LiNO_3$ solution	235.4	230.5 (100th) at 150 mA g^{-1}
$Ag_{0.33}V_2O_5$[29]	nanowires	calomel electrode	5 mol/L $LiNO_3$ + 0.001 mol/L LiOH	103.2	73.7 (50th) at 60 mA g^{-1}
NaV_6O_{15}[30]	micro/nanosheet	$LiMn_2O_4$	saturated $LiNO_3$ solution	162.9	73.1 (100th) at 60 mA g^{-1}

Scheme 1. Schematic Diagram of the Synthesis Process and Study on the Electrochemical Performance of KVO and KVO/GO ARLBs

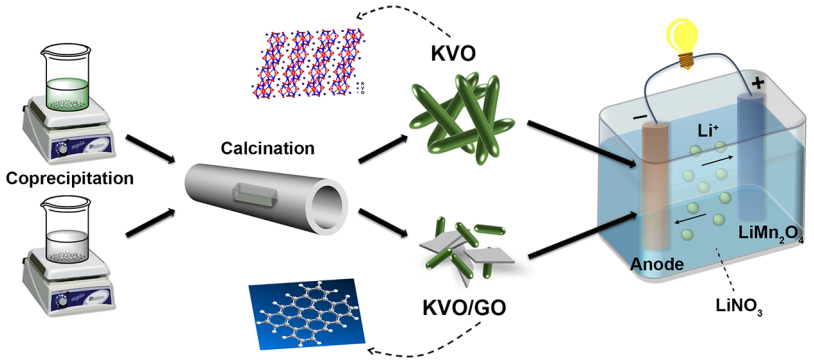

nanobelts by a hydrothermal route, which showed high electrical conductivity that could improve their Li-ion insertion/extraction kinetics.[22] Other various anode materials used with vanadate are listed in Table 1, and corresponding morphologies and electrochemical properties are summarized.[20−30] As far as we can see, previous research on vanadate as an anode material in ARLBs showed either a low discharge capacity or a difficulty in quick charge and discharge at a high current density.

On the one hand, superior anode materials were selected to improve electrochemical properties, such as potassium vanadate, which had a high theoretical capacity and good cycling performance. There have already been some reports about potassium vanadate used as electrode materials.[31,32] On the other hand, carbonaceous materials were used as modified materials to provide a buffer layer for the volume change of anode materials during the lithium-ion insertion/extraction.[33,34] It is worth mentioning that graphene with a high electrical conductivity, high surface area, and excellent mechanical performance has become a popular material to use in batteries.[35,36] In particular, graphene oxide (GO) as the product of oxidation has more abundant functional groups on the surface, which results in a higher activity.[37−39] However, research on an anode modified by GO is insufficient and needs further exploration.

In this paper, $K_{0.25}V_2O_5$ and $K_{0.25}V_2O_5$/GO were prepared by a facile chemical coprecipitation method and a further calcination process. The as-obtained products were used as anode materials along with $LiMn_2O_4$ as a cathode material in the ARLB. The schematic diagram of the synthesis process and study on the electrochemical performance of KVO and KVO/GO ARLB is shown in Scheme 1. The $K_{0.25}V_2O_5$//$LiMn_2O_4$ ARLB exhibited high discharge capacity and good cycling performance at a high current density, while the $K_{0.25}V_2O_5$/GO//$LiMn_2O_4$ ARLB obviously improved the discharge capacity and rate capability. We also investigated the effect of different amounts of graphene oxide on electrochemical performance. Therefore, this work on special vanadate modified by GO as anodes provided a new idea for the development and application in the battery industry.

2. EXPERIMENTAL SECTION

2.1. Materials. Vanadium pentoxide (V_2O_5), potassium vanadate (KVO_3), hydrogen peroxide (H_2O_2, 30 wt %), and graphene oxide were purchased from Aladdin (Shanghai, China). All chemicals were directly used as received without any further purification.

2.2. Methods. *2.2.1. $K_{0.25}V_2O_5$.* $K_{0.25}V_2O_5$ powder was prepared by a facile coprecipitation method and a subsequent calcination process. V_2O_5 and KVO_3 with a molar ratio of 3.5:1 were dissolved in 10 mL of deionized water, and then, 30 mL of H_2O_2 was dropwise added into the solution under magnetic stirring. A fast and exothermic reaction took place to produce the dark green precipitate. The as-obtained precipitate was washed several times with deionized water by vacuum filtration. Finally, the precursor was heated at 600 °C for 5 h in a flowing argon atmosphere, and $K_{0.25}V_2O_5$ (KVO) was prepared.

2.2.2. $K_{0.25}V_2O_5$/GO. $K_{0.25}V_2O_5$/GO powder was prepared similarly according to the way mentioned above. During the

https://doi.org/10.1021/acsomega.2c02833
ACS Omega 2022, 7, 35552−35561

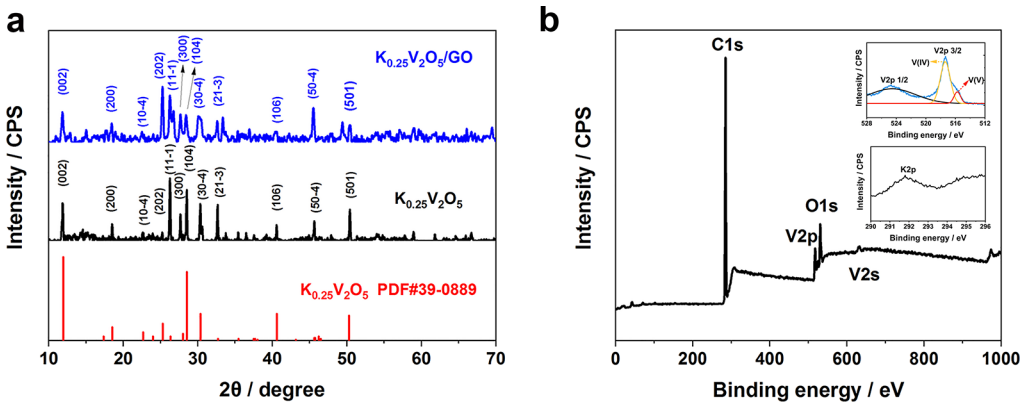

Figure 1. (a) XRD patterns of KVO and KVO/GO and (b) XPS spectra of the KVO and high-resolution spectra of K and V (inset).

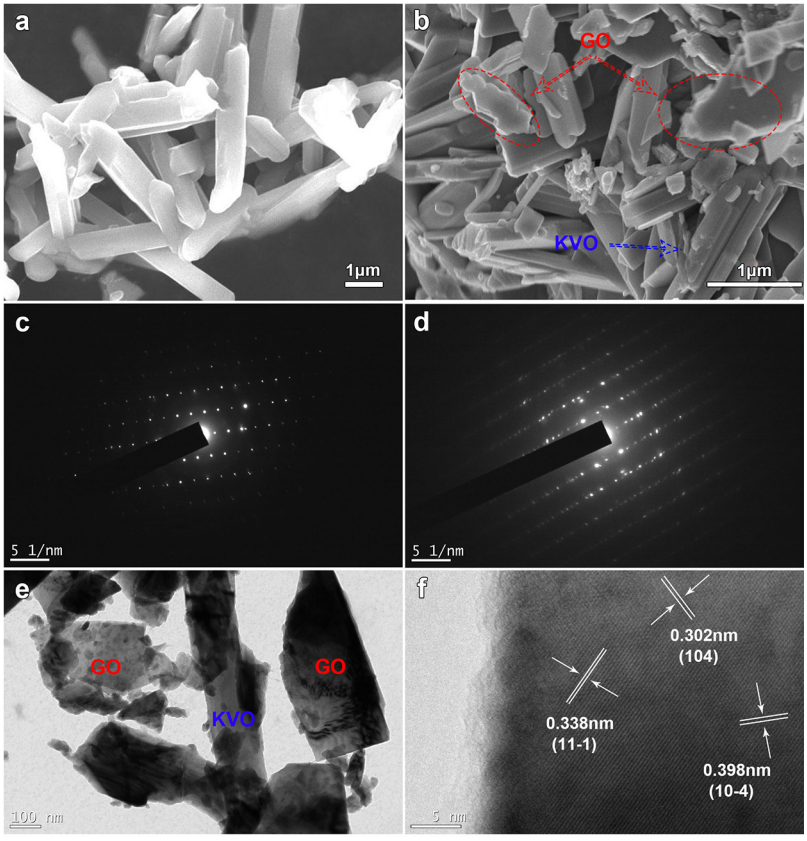

Figure 2. SEM and TEM images. (a) SEM image of KVO, (b) SEM image of KVO/GO, (c) SAED of KVO, (d) SAED of KVO/GO, and (e) TEM image and (f) HRTEM image of KVO/GO.

process, 1 wt % graphene oxide was added into the above solution. The as-obtained product was heated at 600 °C for 5 h in a flowing argon atmosphere, and $K_{0.25}V_2O_5$/GO (KVO/GO) was synthesized.

2.3. Characterization and Measurements. The morphologies of the as-prepared products were characterized by field-emission scanning electron microscopy (FESEM, JEOL JEM-7000F, Japan) at an acceleration voltage of 15.0 kV and transmission electron microscopy (TEM, JEOL JEM-2100, Japan) at 200 kV. The phases and the crystalline structures were investigated by X-ray diffraction (D8 ADVANCE A25, Germany; Cu Kα, λ = 0.15418 nm) whose 2θ ranged from 10 to 70° with a speed of 5° min^{-1}. X-ray photoelectron spectroscopy (XPS) was measured by a Thermo Fisher Scientific ESCALAB Xi+.

The ARLB system was self-assembled, and the reference electrode (RE) and the counter electrode (CE) were a saturated calomel electrode (SCE) and $LiMn_2O_4$, respectively. The working electrode (WE) was fabricated with the as-prepared materials, acetylene black and PVDF with a weight ratio of 8:1:1, which were dissolved in *N*-methylpyrrolidone. The black slurry was uniformly mixed by an ultrasonic method for 1 min, and then, we coated it on a nickel mesh followed by drying at 100 °C for 10 h under vacuum. The electrolyte was saturated $LiNO_3$. The real testing picture of the self-assembled three-electrode ARLB is shown in the Supporting Information.

https://doi.org/10.1021/acsomega.2c02833
ACS Omega 2022, 7, 35552−35561

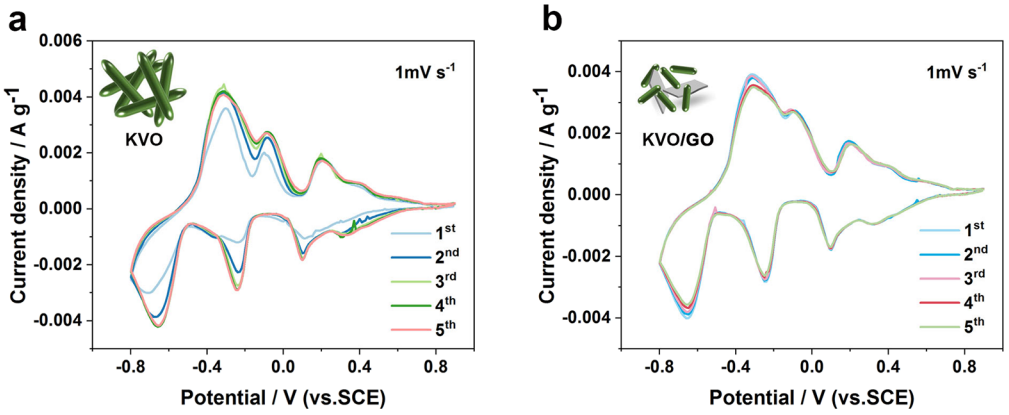

Figure 3. CV curves of (a) KVO and (b) KVO/GO at a scan rate of 1 mV s^{-1}.

The electrochemical properties were tested by an Arbin BT2000 instrument and controlled by Arbin MITS Pro software. CV curves were examined by an AMETEK VMC-4 system at different scanning rates with a scanning voltage range from −0.8 to 0.9 V (vs SCE). EIS was measured within the scanning frequency range from 10^{-2} to 10^{5} Hz using an AMETEK VMC-4 in the aqueous electrolyte. All tests were carried out at room temperature.

3. RESULTS AND DISCUSSION

The X-ray diffraction patterns of KVO and KVO/GO are shown in Figure 1a. The characteristic diffraction peaks corresponding to the (002), (200), (202), (11$\bar{1}$), (300), (104), (30$\bar{4}$), (21$\bar{3}$), (106), (50$\bar{4}$), and (501) planes were fully matched to $K_{0.25}V_2O_5$ (PDF no. 39-0889), which indicated that both KVO and KVO/GO were completely crystallized in accordance with the monoclinic $K_{0.25}V_2O_5$ crystalline phase. There was neither a significant peak shift nor sharp peaks indexed to carbon in the KVO/GO pattern, which demonstrated that carbon derived from graphene oxide existed as an amorphous state.

The XPS analysis was carried out to further investigate the chemical state of the as-synthesized KVO. As shown in Figure 1b, the binding energy was corrected to 284.8 eV by referring to C 1s. The XPS spectrum proved that the as-prepared KVO contained potassium, vanadium, and oxygen, and there was no impurity element discovered. The weak peak at 291 eV pointed to K 2p, while the sharp peak at 530 eV of O 1s binding energy meant that oxygen atoms existed as O^{2-} in the KVO. The V $2p_{3/2}$ and V $2p_{1/2}$ peaks at 517.35 and 524.65 eV well-illustrated that there was V^{5+} existing in the KVO. In addition, the V $2p_{3/2}$ peak at 515.65 eV could be indexed to V^{4+}, which revealed that both V^{4+} and V^{5+} were present to form V in the as-synthesized KVO.

The morphology was investigated by SEM and TEM in Figure 2. Figure 2a exhibits a uniform rod-like structure of KVO, whose length was several micrometers. However, a mixture of the rod-like KVO and sheet-shape graphene oxide was observed in the KVO/GO composites, as shown in Figure 2b. The KVO in the KVO/GO showed a smaller size than single KVO, which may be caused by the effect of graphene oxide on nucleation and growth of KVO. As a result, the addition of graphene oxide changed the microlength of $K_{0.25}V_2O_5$ to nanoscale rods. The as-prepared KVO indicated the single crystalline nature from the SAED pattern in Figure 2c, and the KVO/GO was also single crystals, but there were some messy diffraction spots shown in Figure 2d, which resulted from the amorphous graphene oxide. KVO/GO shows randomly oriented nanorods and graphene oxide forming a homogeneous three-dimensional (3D) stack nanostructure in Figure 2e, and such a nanorod morphology is conducive to a higher surface area, which gives better contact with the electrolyte in order to improve the lithium-ion conductivity. Furthermore, a representative HRTEM image of a microstructure in Figure 2e showed that the lattice fringe spacings were about 0.338, 0.302, and 0.398 nm, which correspond to the interplanar distances of the (11$\bar{1}$), (104), and (10$\bar{4}$) planes of KVO/GO.

Figure 3 shows the typical cyclic voltammetry curves in the voltage range between −0.8 and 0.9 V (vs SCE) at a scan rate of 1 mV s^{-1}. Both KVO (Figure 3a) and KVO/GO (Figure 3b) exhibited three pairs of the main reversible oxidation/reduction peaks located at 0.21/0.18, −0.12/−0.32, and −0.35/−0.7 V, which was ascribed to the multistep lithium-ion insertion/extraction process. After the 5th cycle, CV curves of KVO/GO showed better reversibility because these nanorod-like composites provided a stable structure for lithium-ion insertion/extraction. This assumption was further confirmed by subsequent impedance spectroscopy and the calculated Li^+ diffusion coefficient.

In order to understand the effect of lithium-ion diffusion on electrochemical properties, EIS testing was carried out using KVO and KVO/GO as anodes, whose EIS Nyquist patterns are shown in Figure 4a,b. As far as it can be seen, Nyquist patterns consisted of two parts, where there was an arc in the high frequency range corresponding to charge transfer resistance of the electrode reaction but a line in the low frequency range related to Warburg impedance of the lithium ions from the electrolyte interface to the interior of materials. The larger semicircle in Figure 4a meant the larger transfer resistance between the electrolyte and active KVO materials, while the smaller semicircle in Figure 4b meant the smaller transfer resistance between the electrolyte and active KVO/GO materials. To further analyze the electrochemical properties of KVO and KVO/GO, we used ZView2 software to fit the EIS patterns. The equivalent circuit to fit the impedance data is drawn in Figure 4c, in which the constant-phase element (CPE) representing the double-layer capacitance between the electrode materials and the electrolyte, transfer resistance (R_{ct}), and internal impedance (R_s) were obtained from Figure 4a,b. As we could see, KVO/GO had lower R_{ct} and R_s values due to the addition of GO.

https://doi.org/10.1021/acsomega.2c02833
ACS Omega 2022, 7, 35552−35561

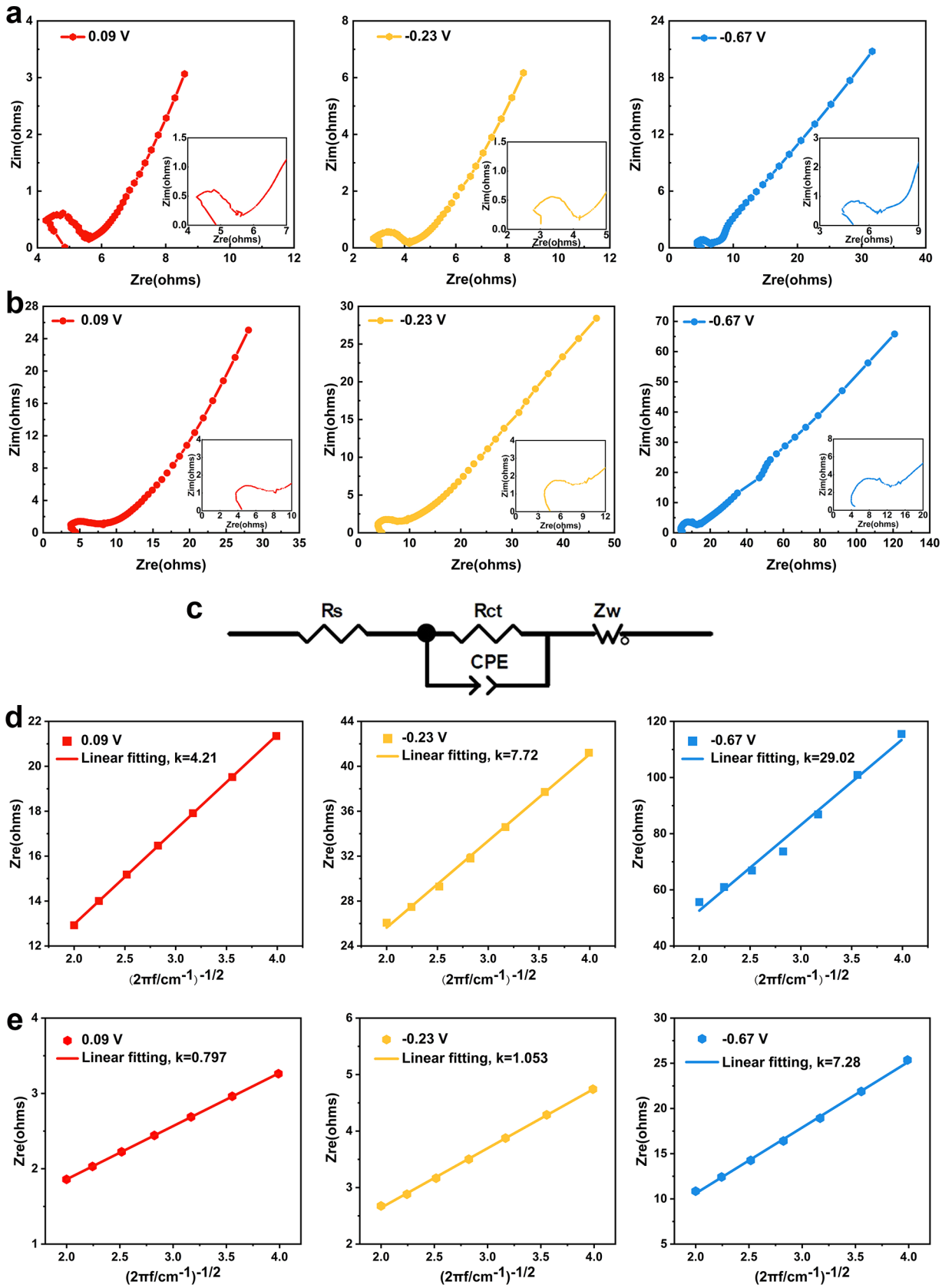

Figure 4. EIS Nyquist patterns of (a) KVO and (b) KVO/GO, (c) equivalent circuit model, and fitting lines of the relationship between Z_{re} and $\omega^{-1/2}$ of (d) KVO and (e) KVO/GO (a_1, b_1, d_1, and e_1: 0.09 V; a_2, b_2, d_2, and e_2: −0.23 V; a_3, b_3, d_3, and e_3: −0.67 V).

The theoretical discharge capacity was 419 mAh g^{-1} when Li^+ was inserted into the cell of KVO, whose detailed calculation process is shown in the Supporting Information. The number of Li^+ insertion during different stages was

https://doi.org/10.1021/acsomega.2c02833
ACS Omega 2022, 7, 35552−35561

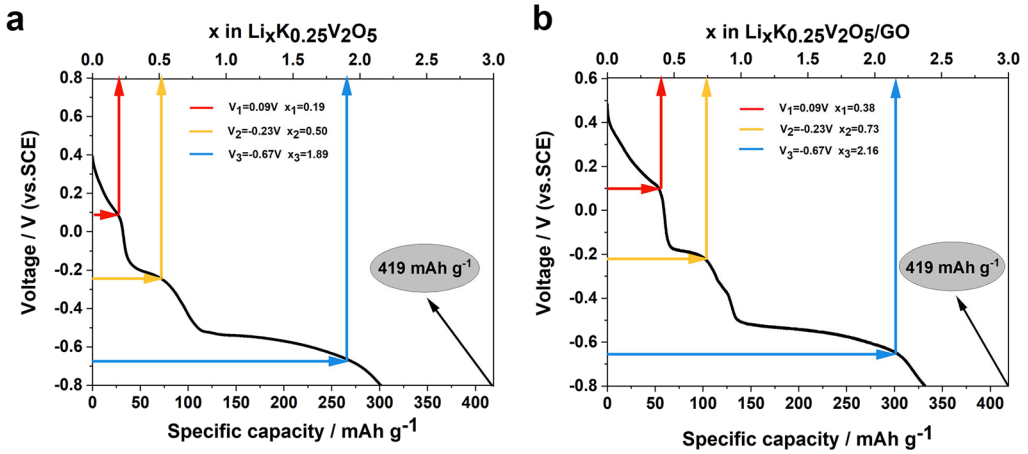

Figure 5. Lithium-ion concentration as a function of discharge plateaus for (a) KVO and (b) KVO/GO.

Table 2. Parameters of the Fitted Circuit and the Lithium-Ion Diffusion Coefficient

material	potential (V) vs SCE	R_s (Ω)	R_{ct} (Ω)	CPE	$Z_w - R$ (Ω)	lithium-ion diffusion coefficient
KVO	0.09	2.519	4.207	0.607	12.98	7.209×10^{-11}
	−0.23	2.133	3.15	0.761	21.9	3.330×10^{-12}
	−0.67	1.812	4.516	0.978	28.24	1.913×10^{-14}
KVO/GO	0.09	3.736	1.591	0.752	1.976	3.084×10^{-9}
	−0.23	2.554	1.341	0.803	2.126	4.851×10^{-10}
	−0.67	2.855	2.447	0.717	37.54	1.314×10^{-12}

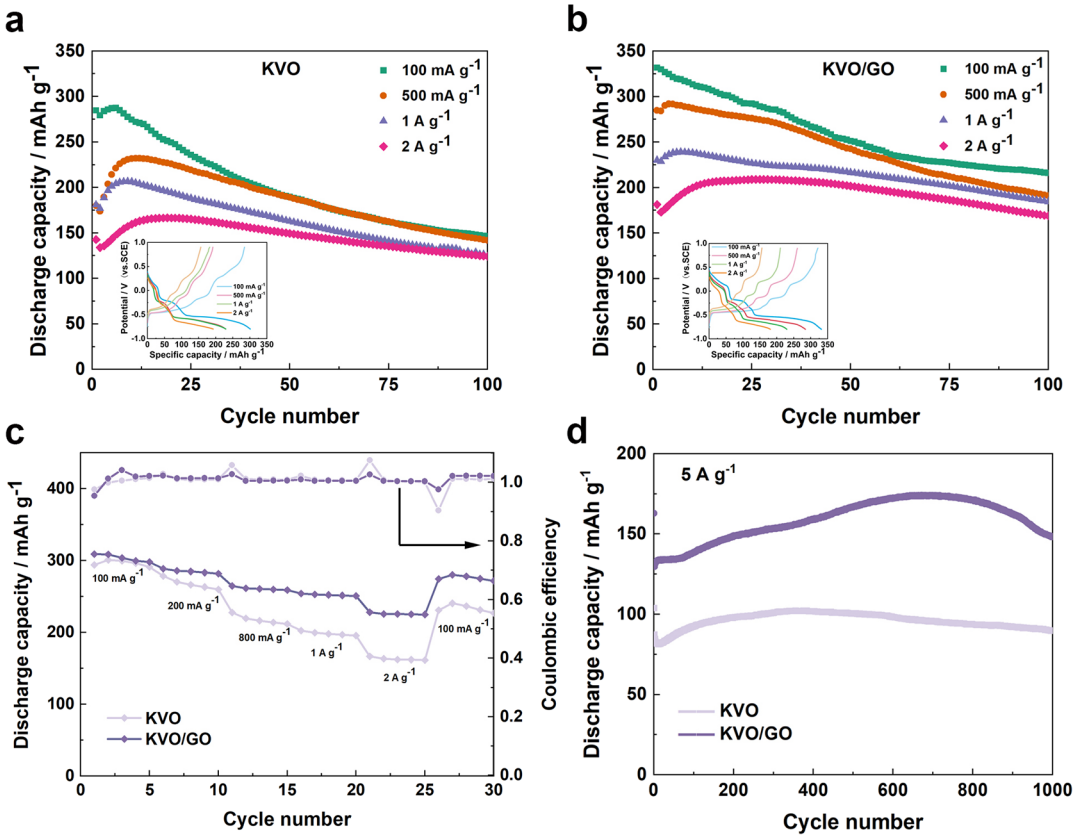

Figure 6. Cycling behaviors of (a) KVO//$LiMn_2O_4$//$LiNO_3$ and (b) KVO/GO//$LiMn_2O_4$//$LiNO_3$ ARLBs at 100, 500, 1000, and 2000 mA g^{-1}, with the inset of the 1st charge/discharge curves; (c) rate capability and Coulombic efficiency of KVO and KVO/GO at rates of 100, 200, 800, 1000, 2000, and 100 mA g^{-1}; (d) super long cycling performance of KVO and KVO/GO at a high current density of 5 A g^{-1}.

obtained through the analysis of the discharge voltage platform in the discharge curves. As could be seen in Figure 5a, the numbers of Li^+ insertion in KVO were about 0.19, 0.50, and 1.89 corresponding to voltages of 0.09, −0.23, and −0.67 V,

https://doi.org/10.1021/acsomega.2c02833
ACS Omega 2022, 7, 35552−35561

respectively, which are close to the number of Li^+ insertion in the traditional organic electrolyte. However, the numbers of Li^+ insertion in KVO/GO were about 0.38, 0.73, and 2.16, respectively, which are a big promotion, as shown in Figure 5b. It was revealed that the introduction of graphene oxide could change the structure of materials and activate more sites for lithium insertion, which improved the capacity performance. The lithium-ion concentration (C) at different stages was calculated according to the following formula:

$$C = \frac{x}{V_m} \quad (1)$$

where x is the number of Li^+ insertion; V_m is the molar volume of KVO, which could be calculated by the standard PDF card of XRD patterns, where V_m = 54.35 cm^3/mol.

The lithium-ion diffusion coefficient (D_{Li^+}) could be calculated according to the following formula:

$$D_{Li^+} = \frac{R^2T^2}{2A^2N^4F^4C^2\sigma^2} \quad (2)$$

where R is the gas constant (8.314 J mol^{-1} K^{-1}); T is the thermodynamic temperature (298.15 K); A is the cross-sectional area between the electrode and the electrolyte (cm^2); N is the electron transfer number of the electrode reaction; F is the Faraday constant (96,485.33 C mol^{-1}); C is the lithium-ion concentration; σ is the Warburg coefficient.

The Warburg coefficient (σ) is related to the real part of the Warburg impedance (Z_{re}), and the corresponding mass transfer process of Li^+ can be described as follows:

$$Z_{re} = R_s + R_{ct} + \sigma\omega^{-1/2} \quad (3)$$

where Z_{re} is the real part of the impedance (Ω); R_s is the solution resistance between the cathode and the anode (Ω); R_{ct} is the transfer resistance (Ω); ω is the angular frequency.

From the fitting patterns in Figure 4d,e, the slope σ could be obtained from the linear relationship between Z_{re} and $\omega^{-1/2}$. The corresponding parameters for calculating D_{Li^+} are listed in Table 2. The results showed that D_{Li^+} of both KVO and KVO/GO ARLB was higher than that of a traditional LIB whose characteristic is beneficial for the ARLB to have high rate performance. The D_{Li^+} values of KVO at 0.09, −0.23, and −0.67 V were 7.209×10^{-11}, 3.330×10^{-12}, and 1.913×10^{-14}, respectively. However, the D_{Li^+} values of KVO/GO at 0.09, −0.23, and −0.67 V were 3.084×10^{-9}, 4.851×10^{-10}, and 1.314×10^{-12}, respectively. From the results, it was not difficult to find that D_{Li^+} of KVO/GO was two orders of magnitude higher than that of KVO, indicating that the introduction of graphene oxide accelerated the diffusion of lithium ions and promoted the electrode reaction kinetics, further improving their electrochemical performance in the ARLB.

The cycling performance and rate capability of KVO and KVO/GO ARLBs were studied. Figure 6a,b shows the cycle behavior of KVO and KVO/GO. In Figure 5a, KVO arrived at a high discharge capacity after 5−10 cycles, and the discharge capacity was 287 mAh g^{-1} at 100 mA g^{-1}, 232 mAh g^{-1} at 500 mA g^{-1}, 206 mAh g^{-1} at 1 A g^{-1}, and 159 mAh g^{-1} at 2 A g^{-1}. The KVO ARLB presented a high capacity but rapid capacity decay, namely, 49% decay at 100 mA g^{-1} after 100 cycles. When it came to KVO/GO, the discharge capacity of the KVO/GO ARLB was improved to 321, 291, 239, and 200 mAh g^{-1} at 100, 500, 1000, and 2000 mA g^{-1}. Compared with KVO, the activation process of the KVO/GO ARLB was shortened, and evidence could be found from Figure 6b in which the discharge capacity reached the maximum after about 5 cycles. In other words, KVO/GO as an anode was much more active than the KVO material. Furthermore, the discharge capacity of the KVO/GO ARLB was reduced to 216, 190, 184, and 168 mAh g^{-1} at 100, 500, 1000, and 2000 mA g^{-1} after 100 cycles, which are much higher than the values of the KVO ARLB. The KVO/GO had a high capacity retention, particularly at a large current density, namely, 84% after 100 cycles at 2000 mA g^{-1}. KVO modified by graphene oxide exhibited the better cycling behavior owing to the smaller size and the lower impedance of the material used. In addition, the 1st charge/discharge curves of the ARLB were investigated in the inset of Figure 6a,b, suggesting that there was multistep process of lithium-ion insertion/extraction. From the analysis of EIS patterns, we also obtained that the charge/discharge platforms of both KVO and KVO/GO corresponded to the redox peaks of CV curves.

Moreover, the rate capability of the KVO and KVO/GO ARLBs was also evaluated through increasing the current density step by step from 100, 200, 800, and 1000 to 2000 mA g^{-1} and finally back to 100 mA g^{-1}. The rate performance of the ARLB of the two different anode materials, KVO and KVO/GO, was tested under the same condition. As shown in Figure 6c, the rate capability of the KVO ARLB was 300, 278, 227, 202, and 166 mAh g^{-1} at 100, 200, 800, 1000, and 2000 mA g^{-1}, respectively. The capacity remained only 226 mAh g^{-1} after the last five cycles, which has a less ideal capacity retention of 75.3%. The KVO/GO ARLB, by contrast, displayed higher capacities with 308, 288, 264, 254, and 227 mAh g^{-1} at current densities of 100, 200, 800, 1000, and 2000 mA g^{-1}. The discharge capacity was slightly reduced to 280 mAh g^{-1} after 25 cycles with a retention of 90.9% while the current density was back to 100 mA g^{-1}, which illustrated that KVO modified by graphene oxide could obviously improve the rate performance and its electrochemical performance was more stable. Additionally, both KVO and KVO/GO ARLBs exhibited a good Coulombic efficiency with almost 100%, indicating that there was almost no reversible capacity loss during the initial charge and discharge process. The long cycling performance of KVO and KVO/GO at a high current density of 5 A g^{-1} was also investigated, which could be observed in Figure 6d. The initial discharge capacity of the KVO ARLB was 82 mAh g^{-1}, while the discharge capacity of the KVO/GO ARLB was 132 mAh g^{-1} at a high current density of 5A g^{-1}. After 1000 cycles, the discharge capacity remained 89 and 148 mAh g^{-1} for the KVO and KVO/GO ARLB, respectively. The good electrochemical performance of KVO/GO was primarily attributed to three factors. First, KVO had a special layered crystalline structure. There were some V−O bonds in the layer, and K^+ existed between the layers. Herein, K^+ provided a strong pillar effect effectively between the vanadium oxide layers and could adjust the structure of the V−O layer to prevent collapse and stabilize the structure during the lithium-ion insertion/extraction.[40] Second, the smaller nanosize of KVO/GO guaranteed a high surface area, which facilitated the adequate contact between the anode and the electrolyte. Finally, plenty of oxygen-based functional groups were introduced into each layer of graphene oxide with a layered structure, which provided more convenient pathways for lithium-ion insertion/extraction in the nanorod-like KVO/GO electrode materials.[37−39] As a result, the lithium-ion

https://doi.org/10.1021/acsomega.2c02833
ACS Omega 2022, 7, 35552−35561

conductivity was improved and so was the electrochemical properties.

In addition, the cycle performance of KVO/GO with different amounts of graphene oxide was investigated to understand the effect of added graphene oxide on electrochemical properties, as shown in Figure 7. The amount of graphene oxide was changed from 1 (KVO/GO1) and 5 (KVO/GO5) to 7% (KVO/GO7), and the corresponding rate capability at rates of 100, 200, 800, 1000, 2000, and back to 100 mA g^{-1} could be observed in Figure 7a. As far as the Coulombic efficiency was concerned, KVO/GO1, KVO/GO5, and KVO/GO7 after modifying by graphene oxide remained almost 100%. However, KVO/GO1, compared with KVO/GO5 and KVO/GO7, presented a higher capacity and more stable performance at the cycling current density. Moreover, the capacity retention of KVO/GO1 attained 90.9%, while KVO/GO5 and KVO/GO7 retained 81.5 and 81.4% (Figure 7b). We also studied the discharge capacity of KVO/GO1, KVO/GO5, and KVO/GO7 from the 1st to 100th cycle at different current densities, which is shown in Figure 7c. As could be seen from the curves, the discharge capacity of KVO/GO1 always behaved better than those of KVO/GO5 and KVO/GO7 at any current density. These results showed that a small amount of graphene oxide added could improve the discharge capacity and cycling stability. A small addition of graphene oxide changed the size of KVO and increased the specific surface area exactly as it was analyzed above, which benefited the insertion and extraction of Li^+. However, excess graphene oxide reduced the electrical conductivity, leading to fading electrochemical performance.

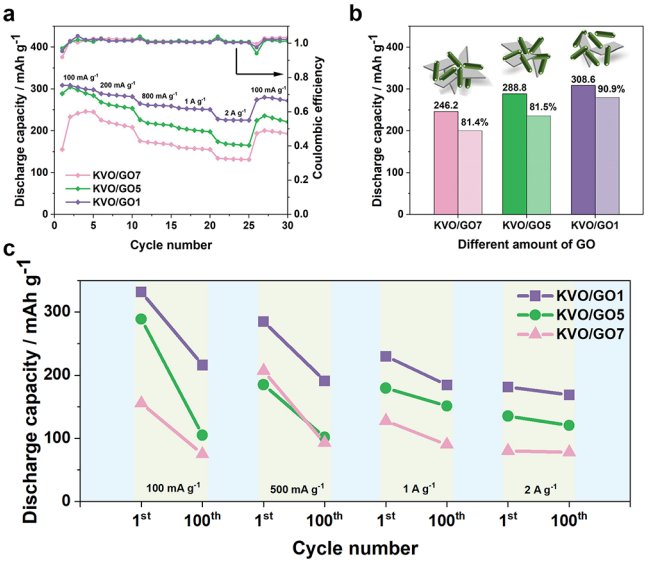

Figure 7. (a) Rate capability and Coulombic efficiency at rates of 100, 200, 800, 1000, 2000, and 100 mA g^{-1}; (b) capacity retention; (c) discharge capacity at the 1st and 100th cycle at 100, 500, 1000, and 2000 mA g^{-1} of KVO/GO1, KVO/GO5, and KVO/GO7.

4. CONCLUSIONS

$K_{0.25}V_2O_5$ and $K_{0.25}V_2O_5$/GO were successfully synthesized by a facile chemical coprecipitation method and a subsequent calcinations process. The as-prepared materials were used as anodes with $LiMn_2O_4$ as a cathode and saturated $LiNO_3$ as an electrolyte in the ARLB to study their electrochemical performance. The results indicated that the electrochemical performance of $K_{0.25}V_2O_5$ modified by graphene oxide was improved compared with $K_{0.25}V_2O_5$, mainly due to the addition of graphene oxide, which not only reduced the size of $K_{0.25}V_2O_5$ rods but also introduced the multilayered structure, leading to an increased specific surface area and channels for the lithium-ion diffusion during the charge/discharge process. In our ARLB system, KVO/GO as an anode exhibited a higher lithium-ion diffusion coefficient, better cycling stability, and rate performance. The addition of graphene oxide could not only improve the initial discharge capacity of the KVO ARLB but also maintained a high capacity retention at a large current density. Furthermore, a small amount of graphene oxide added could improve the electrochemical performance better than excess graphene oxide. Therefore, our study on KVO and KVO/GO materials is of crucial importance for the ARLB to be applied in large-scale power sources and energy storage devices.

■ ASSOCIATED CONTENT

Supporting Information

The Supporting Information is available free of charge at https://pubs.acs.org/doi/10.1021/acsomega.2c02833.

Real testing picture of the self-assembled three-electrode aqueous lithium-ion battery and additional calculation process of theoretical discharge capacity (PDF)

■ AUTHOR INFORMATION

Corresponding Authors

Yanlin Li − *School of Materials Science and Engineering, Xi'an University of Architecture & Technology, Xi'an 710055, China*; orcid.org/0000-0002-5502-7396; Email: liyanlin@xauat.edu.cn

Yuzhen Zhao − *Xi'an Key Laboratory of Advanced Photoelectronics Materials and Energy Conversion Device, Xijing University, Xi'an 710123, China*; Email: zyz19870226@163.com

Zongcheng Miao − *School of Artificial Intelligence, Optics and Electronics (iOPEN), Northwestern Polytechnical University, Xi'an 710072, China*; Email: miaozongcheng@nwpu.edu.cn

Authors

Wenyuan Duan − *Xi'an Key Laboratory of Advanced Photoelectronics Materials and Energy Conversion Device, Xijing University, Xi'an 710123, China*

Youyang Zhao − *Xi'an Key Laboratory of Advanced Photoelectronics Materials and Energy Conversion Device, Xijing University, Xi'an 710123, China*

Huimin Zhang − *Xi'an Key Laboratory of Advanced Photoelectronics Materials and Energy Conversion Device, Xijing University, Xi'an 710123, China*

Jiao Liu − *Xi'an Key Laboratory of Advanced Photo-electronics Materials and Energy Conversion Device, Xijing University, Xi'an 710123, China*

Complete contact information is available at: https://pubs.acs.org/10.1021/acsomega.2c02833

Notes

The authors declare no competing financial interest.

https://doi.org/10.1021/acsomega.2c02833
ACS Omega 2022, 7, 35552−35561

■ ACKNOWLEDGMENTS

This work was supported by the National Natural Science Foundation of China (no. 52173263), the Natural Science Foundation of Anhui Province, China (no. 2108085J11), the Regional Innovation Capability Guidance Program of Shaanxi (no. 2022QFY03-02), and the Fundamental Research Funds for the Central Universities, Northwestern Polytechnical University (no. D5000210825). It was also supported by the Natural Science Basic Research Plan in Shaanxi Province of China (no. 2022GY-380). We acknowledge the testing and analysis from the Xi'an Key Laboratory of Advanced Photoelectronics Materials and Energy Conversion Device in Xijing University (China) and the Key Laboratory of Advanced Functional Materials and Mesoscopic Physics in Xi'an Jiaotong University (China).

■ REFERENCES

(1) Cheng, J.; Hou, G.; Sun, Q.; Liang, Z.; Xu, X.; Guo, J.; Dai, L.; Li, D.; Nie, X.; Zeng, Z.; Si, P.; Ci, L. Cold-pressing PEO/LAGP composite electrolyte for integrated all-solid-state lithium metal battery. *Solid State Ionics* **2020**, *345*, 115156−115162.

(2) He, X.; Yan, B.; Zhang, X.; Liu, Z.; Bresser, D.; Wang, J.; Wang, R.; Cao, X.; Su, Y.; Jia, H.; Grey, C. P.; Frielinghaus, H.; Truhlar, D. G.; Winter, M.; Li, J.; Paillard, E. Fluorine-free water-in-ionomer electrolytes for sustainable lithium-ion batteries. *Nat. Commun.* **2018**, *9*, 5320−5327.

(3) Zhang, H.; Wang, L.; He, X. Trends in a study on thermal runaway mechanism of lithium-ion battery with $LiNi_xMn_yCo_{1-x-y}O_2$ cathode materials. *Battery Energy* **2022**, *1*, 20210011.

(4) Guo, Y.; Zhang, Y.; Lu, H. Manganese-based materials as cathode for rechargeable aqueous zinc-ion batteries. *Battery Energy* **2022**, *1*, 20210014.

(5) Alias, N.; Mohamad, A. A. Advances of aqueous rechargeable lithium-ion battery: A review. *J. Power Sources* **2015**, *274*, 237−251.

(6) Zhang, X.-Q.; Chen, X.; Cheng, X.-B.; Li, B.-Q.; Shen, X.; Yan, C.; Huang, J.-Q.; Zhang, Q. Highly Stable Lithium Metal Batteries Enabled by Regulating the Solvation of Lithium Ions in Nonaqueous Electrolytes. *Angewandte Chemie-International Edition* **2018**, *57*, 5301−5305.

(7) Tron, A.; Park, Y. D.; Mun, J. AlF_3-coated $LiMn_2O_4$ as cathode material for aqueous rechargeable lithium battery with improved cycling stability. *J. Power Sources* **2016**, *325*, 360−364.

(8) Yang, Q.; Wang, W.; Li, H.; Zhang, J.; Kang, F.; Li, B. Investigation of iron hexacyanoferrate as a high rate cathode for aqueous batteries: Sodium-ion batteries and lithium-ion batteries. *Electrochim. Acta* **2018**, *270*, 96−103.

(9) Wang, J.; Lu, X.; Zhang, Y.; Zhou, J.; Wang, J.; Xu, S. Grain size regulation for balancing cycle performance and rate capability of $LiNi_{0.9}Co_{0.055}Mn_{0.045}O_2$ single crystal nickel-rich cathode materials. *J. Energy Chem.* **2022**, *65*, 681−687.

(10) Qi, W.; Ben, L.; Yu, H.; Zhan, Y.; Zhao, W.; Huang, X. Improving the electrochemical cycling performance of anode materials via facile in situ surface deposition of a solid electrolyte layer. *J. Power Sources* **2019**, *424*, 150−157.

(11) Ramanujapuram, A.; Yushin, G. Understanding the Exceptional Performance of Lithium-Ion Battery Cathodes in Aqueous Electrolytes at Subzero Temperatures. *Adv. Energy Mater.* **2018**, *8*, 1802624−1802631.

(12) Hadouchi, M.; Koketsu, T.; Hu, Z.; Ma, J. The origin of fast-charging lithium iron phosphate for batteries. *Battery Energy* **2022**, *1*, 20210010.

(13) Guo, Z.; Chen, L.; Wang, Y.; Wang, C.; Xia, Y. Aqueous Lithium-Ion Batteries Using Polyimide-Activated Carbon Composites Anode and Spinel $LiMn_2O_4$ Cathode. *ACS Sustainable Chem. Eng.* **2017**, *5*, 1503−1508.

(14) Haruna, A. B.; Ozoemena, K. I. Effects of microwave irradiation on the electrochemical performance of manganese-based cathode materials for lithium-ion batteries. *Curr. Opin. Electrochem.* **2019**, *18*, 16−23.

(15) Chen, Y.; Lu, Y.; Liu, Z.; Zhou, L.; Li, Z.; Jiang, J.; Wei, L.; Ren, P.; Mu, T. Efficient Dissolution of Lithium-Ion Batteries Cathode $LiCoO_2$ by Polyethylene Glycol-Based Deep Eutectic Solvents at Mild Temperature. *ACS Sustainable Chem. Eng.* **2020**, *8*, 11713−11720.

(16) Yang, L.; Luo, S.; Wang, Y.; Zhan, Y.; Wang, Q.; Zhang, Y.; Liu, X.; Mu, W.; Teng, F. Excess capacity on compound phases of Li_2FeTiO_4 composite cathode materials synthesized by hydrothermal reaction using optional titanium sources to boost battery performance. *Chin. Chem. Lett.* **2020**, *31*, 3200−3204.

(17) Li, S.-N.; Luo, S.-H.; Yang, L.; Wang, Q.; Zhang, Y.-H.; Liu, X. Synthesis and electrochemical properties of $LiFePO_4$ cathode material by ionic thermal method using eutectic mixture of tetramethyl ammonium chloride-urea. *Rare Met.* **2021**, *40*, 3477−3484.

(18) Chen, H. L.; Cheng, S. L.; Chen, D.; Jiang, Y.; Ang, E. H.; Liu, W. L.; Feng, Y. Z.; Rui, X. H.; Yu, Y. Vanadate-based electrodes for rechargeable batteries. *Mater. Chem. Front.* **2021**, *5*, 1585−1609.

(19) Song, Y.; Wang, T.; Zhu, J.; Liu, Y.; Wang, L.; Dai, L.; He, Z. Recent advances in LiV_3O_8 as anode material for aqueous lithium-ion batteries: Syntheses, modifications, and perspectives. *J. Alloys Compd.* **2022**, *897*, 163065−163078.

(20) Lashari, N. U. R.; Zhao, M.; Zheng, Q.; Gong, H.; Song, X. Good Lithium-Ion Insertion/Extraction Characteristics of a Novel Double Metal Doped Hexa-Vanadate Compounds Used in an Inorganic Aqueous Solution. *Energy Fuels* **2018**, *32*, 10016−10023.

(21) Lashari, N. U. R.; Zhao, M.; Zheng, Q.; Gong, H.; Duan, W.; Xu, T.; Wang, F.; Song, X. Excellent cycling stability and capability of novel mixed-metal vanadate coated with V_2O_5 materials in an aqueous solution. *Electrochim. Acta* **2019**, *314*, 115−123.

(22) Bai, L.; Zhu, J.; Zhang, X.; Xie, Y. Reducing hydrated protons co-intercalation to enhance cycling stability of CuV_2O_5 nanobelts: a new anode material for aqueous lithium ion batteries. *J. Mater. Chem.* **2012**, *22*, 16957−16963.

(23) Sun, D.; Jin, G.; Wang, H.; Liu, P.; Ren, Y.; Jiang, Y.; Tang, Y.; Huang, X. Aqueous rechargeable lithium batteries using NaV_6O_{15} nanoflakes as high performance anodes. *J. Mater. Chem. A* **2014**, *2*, 12999−13005.

(24) Wang, G. J.; Zhang, H. P.; Fu, L. J.; Wang, B.; Wu, Y. P. Aqueous rechargeable lithium battery (ARLB) based on LiV_3O_8 and $LiMn_2O_4$ with good cycling performance. *Electrochem. Commun.* **2007**, *9*, 1873−1876.

(25) Tang, W.; Gao, X.; Zhu, Y.; Yue, Y.; Shi, Y.; Wu, Y.; Zhu, K. A hybrid of V_2O_5 nanowires and MWCNTs coated with polypyrrole as an anode material for aqueous rechargeable lithium batteries with excellent cycling performance. *J. Mater. Chem.* **2012**, *22*, 20143−20145.

(26) Ma, Y.; Wu, M.; Jin, X.; Shu, R.; Hu, C.; Xu, T.; Li, J.; Meng, X.; Cao, X. $(NH_4)_2V_7O_{16}$ Microbricks as a Novel Anode for Aqueous Lithium-Ion Battery with Good Cyclability. *Chem. - Eur. J.* **2021**, *27*, 12341−12351.

(27) Lashari, N. U. R.; Zhao, M.; Zheng, Q.; He, X.; Ahmed, I.; Su, Z.; Tangsee, S.; Song, X. Enhanced Rate Capability and Cycling Stability of Novel Ammonium Vanadate Materials Used in Aqueous Li-Ion Batteries. *Energy Fuels* **2021**, *35*, 4570−4576.

(28) Liu, J.; Yi, L.; Liu, L.; Peng, P. LiV_3O_8 nanowires with excellent stability for aqueous rechargeable lithium batteries. *Mater. Chem. Phys.* **2015**, *161*, 211−218.

(29) Xu, Y.; Han, X.; Zheng, L.; Yan, W.; Xie, Y. Pillar effect on cyclability enhancement for aqueous lithium ion batteries: a new material of beta-vanadium bronze $M_{0.33}V_2O_5$ (M = Ag, Na) nanowires. *J. Mater. Chem.* **2011**, *21*, 14466−14472.

(30) Zhao, M.; Zhang, W.; Song, X. Lithium-ion storage properties of a micro/nanosheet-like NaV_6O_{15} anode in aqueous solution. *Dalton Trans.* **2017**, *46*, 3857−3863.

(31) Baddour-Hadjean, R.; Boudaoud, A.; Bach, S.; Emery, N.; Pereira-Ramos, J.-P. A Comparative Insight of Potassium Vanadates as Positive Electrode Materials for Li Batteries: Influence of the Long-Range and Local Structure. *Inorg. Chem.* **2014**, *53*, 1764−1772.

https://doi.org/10.1021/acsomega.2c02833
ACS Omega 2022, 7, 35552−35561

(32) Fang, G.; Zhou, J.; Hu, Y.; Cao, X.; Tang, Y.; Liang, S. Facile synthesis of potassium vanadate cathode material with superior cycling stability for lithium ion batteries. *J. Power Sources* **2015**, *275*, 694−701.
(33) Fan, L.; Lu, B. Reactive Oxygen-Doped 3D Interdigital Carbonaceous Materials for Li and Na Ion Batteries. *Small* **2016**, *12*, 2783−2791.
(34) Jia, B.-R.; Qin, M.-L.; Zhang, Z.-L.; Li, S.-M.; Zhang, D.-Y.; Wu, H.-Y.; Zhang, L.; Lu, X.; Qu, X.-H. Hollow Porous VOx/C Nanoscrolls as High-Performance Anodes for Lithium-Ion Batteries. *ACS Appl. Mater. Interfaces* **2016**, *8*, 25954−25961.
(35) Zhong, M.; Yan, J.; Wu, H.; Shen, W.; Zhang, J.; Yu, C.; Li, L.; Hao, Q.; Gao, F.; Tian, Y.; Huang, Y.; Guo, S. Multilayer graphene spheres generated from anthracite and semi-coke as anode materials for lithium-ion batteries. *Fuel Process. Technol.* **2020**, *198*, 106241−106248.
(36) Xu, Y.; Lin, Z.; Zhong, X.; Papandrea, B.; Huang, Y.; Duan, X. Solvated Graphene Frameworks as High-Performance Anodes for Lithium-Ion Batteries. *Angewandte Chemie-International Edition* **2015**, *54*, 5345−5350.
(37) Zhang, Y.; Song, N.; He, J.; Chen, R.; Li, X. Lithiation-Aided Conversion of End-of-Life Lithium-Ion Battery Anodes to High-Quality Graphene and Graphene Oxide. *Nano Lett.* **2019**, *19*, 512−519.
(38) Li, C.; Wang, X.; Li, S.; Li, Q.; Xu, J.; Liu, X.; Liu, C.; Xu, Y.; Liu, J.; Li, H.; Guo, P.; Zhao, X. S. Optimization of $NiFe_2O_4$/rGO composite electrode for lithium-ion batteries. *Appl. Surf. Sci.* **2017**, *416*, 308−317.
(39) Kornilov, D.; Penki, T. R.; Cheglakov, A.; Aurbach, D. Li/graphene oxide primary battery system and mechanism. *Battery Energy* **2022**, *1*, 20210002.
(40) Xu, M.; Han, J.; Li, G.; Niu, Y.; Liu, S.; Hou, J.; Wang, M.; Song, J.; Li, C. M. Synthesis of novel book-like $K_{0.23}V_2O_5$ crystals and their electrochemical behavior in lithium batteries. *Chem. Commun.* **2015**, *51*, 15290−15293.

https://doi.org/10.1021/acsomega.2c02833
ACS Omega 2022, 7, 35552−35561